SOI-MDI Technical Notes

Optimal Masks for Structure Program

Version 1.1

A.G. Kosovichev

October 1992

SOI-TN-096

Stanford - Lockheed Institute
for Astrophysical and Space Research

Solar Oscillation Investigation
Michelson Doppler Imager

Optimal Masks for Structure Program

Version 1.1
16 November 1992

A. G. Kosovichev

Institute of Astronomy, University of Cambridge
The Observatories, Madingley Road, Cambridge, CB3 0HA
Center for Space Science and Astrophysics
Stanford University, Stanford, CA 94305-4055
Crimean Astrophysical Observatory
334413 p/o Nauchny, Crimea, Ukraine

Abstract

Optimal masks for the SOI-MDI Structure Program to observe p modes for angular degree value l from 0 to $\sim$ 200 are discussed.

In Section 3.4 of version 1.1 of the notes I present results for corrections of numerical filters, which are applied to binned data in order to extract oscillation eigenmodes, for angles B_0 and δP by using Wigner's D-functions.

An error in a computer code of version 1.0 has been corrected. The error was in miscounting bins in one row resulting in corruption of the previously reported results because of an artificial mode interference.

1 Introduction

The primary objectives of the Structure Program are investigations of radial stratification, internal rotation, large-scale asphericity, internal global fields, large-scale surface flows, and the figure of the limb [1]. At least the first four objectives require observations of frequencies of oscillation modes that are as accurate as possible. Observationaly, accuracy of frequency determination is limited by the duration of uninterrupted time series. Therefore, the data for the structure program must be transmitted continuously in the 5 kbps channel. There is enough telemetry for about 30,000 8-bit numbers per minute.

Helioseismic inversions of existing data have shown that a uniform data set of modes of all angular degrees l and orders m up to some $l_{\max}$ is essential in order to achieve the objectives of the Structure Program. The value of $l_{\max}$ has to be chosen to be about $\sim$200–250 for two main reasons: first, because p modes of l in the range from 0 to 200 sample almost the entire the solar interior from 0 to $0.98R_\odot$ [2]; second, because modes of higher degree cannot be resolved individually, as they are blended into ridges [3]. For the Structure Program, it is very important that the modes of $l \simeq 200$ sample the HeII ionization zone (located at $0.98R_\odot$), which is essential to study the helium abundance and also solar thermodynamics [4] as related to some fundamental aspects of the equation of state, such as atomic energy-level shifts, partition functions of excited atomic states and others. Moreover, the high-l modes are important for determining accurately parameters in the deep solar interior, because they provide information about the surface layers of the sun, to which all the p modes are most sensitive. The influence of the surface layers has to be understood and taken into account in the structure inversions [5,6]. In principle, modes of all values of m for given l are required to study asphericity, internal differential rotation and magnetic fields.

Recent helioseismic inversions [4-6] have also shown the importance of modes of low radial orders n. These modes carry more independent information on solar structure than modes of high n, because the low-n modes are off the p-mode asymptotic regime, where the

frequency information is significantly degenerate (e.g.[2]). The modes have frequencies in the range 1–2 mHz, and they are significantly less affected by turbulent surface layers. It is also important that their lifetime is long enough to resolve individual peaks in rotational frequency splittings. However, the mode amplitudes are substantially lower than those at 3 mHz. Therefore, a good signal-to-noise is required for their observation. Frequencies of the low-degree modes are the most important observables for the Structure Program.

Currently, from the ground, observations of individual p modes have been resolved up to l=120 [7] and 140 [8]. There is evidence for individually resolved modes up to l=190 in recent South Pole data [9]. However, ground observations suffer serious distortion by average terrestrial atmospheric turbulence. For that reason the GONG instrument is planned for l values between 1 and ~150 [10]. Measurement of individual p modes for higher l, up to ~200–250, however, would be an important goal for the space observations.

One of the potential plans that has been discussed for the SOI Structure Program is to project the velocity signal onto a selection of spherical harmonics for transmitting to the ground. Such a procedure has several drawbacks, the most important of which is that symmetry breaking agents in the sun, particularly latitudinal rotational shear, distort the eigenfunctions away from the separable spherical harmonic form. Of course one might contemplate taking that distortion into account in the design of masks, until one realizes that one does not know the differential rotation well enough to do so [11]. But even if one did, there is a further intrinsic difficulty with such a procedure, which cannot be removed so as to yield a mask for an entire sequence of modes of like l and m and varying n: that is, the distortion of the spatial structure of modes varies with frequency, and since modes are finally to be isolated by analysing temporal variation on the ground, single masks to be applied at instants of time (rather than frequency) to isolate modes do not exist. To carry out the task in hand, one would need to combine the outputs from a combination of different masks. Once one has accepted that conclusion, it becomes evident that it is no longer necessary to design masks in such a way that just one of them dominates any process that is later to be carried out on the ground. Hence, one can now entertain satisfying different previously subordinated criteria for optimizing the strategy. In particular, on-board simplicity ranks highly, on grounds of both cost and reliability.

One possible observational scheme, which is suggested here, is to bin the high-resolution data into a single grid of lower-resolution bins, the total number of which is compatible with the 5 kbps telemetry channel, so that the signals from the bins could be brought down via the telemetry channel. In this approach, the entire mode extraction from the data should be carried out on the ground. The central point of the analysis is decomposition of the data onto solar mode eigenfunctions. Therefore, the binned data should provide maximum information about the eigenfunctions. In other words, the problem with which we are faced

is in designing an optimal data binning (optimal masks) for a given number of bins to obtain maximum information about solar oscillations from the ground analysis. An optimal binning procedure has not yet been developed. In the notes we give an example of a mask, which allows observations of modes up to $l_{\max} \sim 200$ with the total number of bins $K_{\rm bin} \simeq 10,000$. We also discuss problems with the procedure, which are being considered.

2 Data binning

2.1 Basic principles of optimal masks

The basic idea is to bin the high-resolution data according to amplitude distribution of the oscillation eigenfunctions on the solar disk. In the first approximation, the eigenfunctions ξ_l^m of p modes can be described in terms of spherical harmonics in the heliospheric coordinates (θ, ϕ):

$$\xi_l^m \sim Y_l^m(\theta, \phi) \equiv \frac{1}{\sqrt{2\pi}} P_l^m(\cos\theta) e^{im\phi}, \tag{1}$$

where $P_l^m(\cos\theta)$ are normalized associated Legendre functions of the first kind, with the normalization relation given by

$$\int_0^\pi [P_l^m(\cos\theta)]^2 \sin\theta d\theta = 1;$$

and the origin of ϕ is taken to be the central meridian. Therefore, the binning should take into account properties of the spherical harmonics. For instance, for a given l the modes with $m \simeq l$ have the smallest wavelength in the ϕ direction, but they are concentrated near the equator, whereas the modes with $m \ll l$ propagate into the polar regions but their azimuthal wavelength is relatively large. Therefore, a high spatial resolution should be kept in the polar direction, but in the azimuthal direction the high resolution is necessary only in an equatorial region and can be significantly degraded towards the poles without losing significant information about the eigenfunctions. In principle, it is possible to develop a procedure for an optimal binning. But that has not yet been done, and here we simply give an example of a binning based on this principle.

2.2 An example of nonuniform binning

We consider possible data binning for a case when we wish to observe modes up to $l_{\max} = 200$ with a maximum number of bins $K_{\rm bin} \simeq 10,000$. The number of the bins k_y in the South-North direction (axis y in a solar image) should be sufficient to resolve the zonal mode of degree $l_{\max}$. We choose $k_y = 192$. It is convenient to design the bin shapes

to projections of latitudes and longitudes onto the solar image. However, for the purpose of binning the data we shall ignore a possible inclination of the solar rotation axis to the plane of the sky in order to avoid time-dependent remapping of the data. The inclination can be taken into account in a numerical procedure of decomposion of the binned data onto spherical harmonics (see Sec.3). In the example, we suppose that the bins are equally spaced in the y-direction. The number k_x of bins in the East-West direction (x axis in the solar image) depends on latitude, and it should be sufficient to resolve completely all sectoral modes ($m = l$). The number of bins at a given colatitude θ_0 can be chosen to be approximately equal to the degree m_0 of the modes that propagate to the colatitude. The mode amplitudes are proportional to $\sin^m \theta$. If we assume that the limits of the propagation region are defined to be the latitudes at which the mode amplitudes do not exceed a factor ϵ of their equatorial amplitudes, then we obtain

$$m_0 = \frac{\log \epsilon}{\log(\sin \theta_0)}. \tag{2}$$

In Figure 1, by thin solid curves, we show m_0 for $\epsilon = 0.1$ as a function of distance y from the projection of the equator on the solar disk. The number of bins k_x in the East-West direction is chosen from an approximation of the curves by a step function m_s(thick solid lines), which means that the solar image is divided into a number of bands (15, in our example) with equal values $k_x = m_s$ in each of them. The projections of latitudes onto the solar disk are ellipses. Therefore, the shapes of the bins can easily be computed by a simple algorithm (Fig.2). In practice, the ellipses could be approximated by step functions to match a pixel configuration of a CCD array. The total number of the bins in our example is equal to 10,464.

2.3 Mode resolution and the number of bins

One can note that the number of bins $K_{\rm bin}$ in the masks is proportional to $l^2_{\rm max}$:

$$K_{\rm bin} = \alpha l^2_{\rm max}. \tag{3}$$

In the above example the coefficient $\alpha \approx 1/4$. This particular mask was designed to register full signals from zonal and sectoral modes, but signals from modes of intermediate azimuthal orders m at high degree $l \simeq l_{\rm max}$ are not registered completely. That implies a partial loss of sensitivity to the modes compared with the full (1024×1024) unbinned data. The significance of the loss of sensitivity for the mode measurements can be estimated from the data analysis (Sec. 3). By increasing the number of bins, it is possible to design masks with a complete coverage of the oscillation eigenfunctions. The colatitudes of turning points of tesseral modes in the polar direction can be determined from an asymptotic approximation

$$\theta_0 = \arcsin \frac{m}{l + 0.5}. \tag{4}$$

Then it is possible to estimate the number of bins as a function of the coordinate y: $m_0 = (l + 0.5)\sin(\arccos y)$ (dashed curves in Fig.1). For this mask the coefficient $\alpha \approx 3/4$. Therefore, the total number of bins is about 30,000.

In practice, a compromise can be chosen between these two extreme cases.

3 Decomposition of binned data into oscillation eigenfunctions

This is an important problem for analysis of the data and for an optimal binning. The basic principle is to find numerical filters to achieve the best separation of an eigenfunction of a given mode both from the other oscillation modes and from noise. Several approaches to optimize the numerical filters have been considered [12-15]. They can be applied to the proposed mask. However, for a first evaluation of mode resolution by the masks we use a simple technique [16] based on an approximate orthogonality of the eigenfunction.

3.1 Sensitivity functions

The first step in the data analysis is to compute the sensitivity of the binning to solar oscillation modes. The sensitivity functions are used in numerical filters to isolate a signal from a given mode.

We assume that the contribution to the velocity field on the solar surface from a mode of radial order n, degree l and azimuthal order m can be described in terms of spherical harmonics:

$$v_{nlm}(\theta,\phi,t) = a_{nlm}\mathrm{Re}\left[e_r Y_l^m(\theta,\phi) + \frac{\alpha_{nlm}}{\sqrt{l(l+1)}}\nabla_\perp Y_l^m(\theta,\phi)\right] e^{-i(\omega_{nlm}t + \epsilon_{nlm})}, \qquad (5)$$

where θ and ϕ are heliospheric coordinates with the polar axis Oz directed along the rotation axis, a_{nlm} is the radial component of the velocity and α_{nlm} is the ratio between the horizontal and radial components, ω_{nlm} is frequency, ϵ_{nlm} is phase of the mode, and

$$\nabla_\perp \equiv e_\theta \frac{\partial}{\partial\theta} + e_\phi \frac{1}{\sin\theta}\frac{\partial}{\partial\phi}.$$

The distortion from symmetry-breaking agents can be accounted for either by perturbation or by asymptotic methods in a more refined analysis. For p modes, the value of α_{nlm} can be estimated as (e.g. [17]):

$$\alpha_{nlm} \simeq \sqrt{l(l+1)}\left(\frac{\omega_0}{\omega_{nlm}}\right)^2, \qquad (6)$$

where $\omega_0/2\pi = \sqrt{GM/R^3}/2\pi \approx 0.1$mHz. Therefore, the horizontal component could be significant for high-degree low-frequency oscillations, for instance, $\alpha_{nlm} \gtrsim 1/4$ for $l \gtrsim 100$ and $\omega_{nlm}/2\pi \lesssim 2$ mHz.

Along with the heliospheric coordinates (r, θ, ϕ), we consider the coordinate system (r, Θ, Φ) whose polar axis OZ is parallel to the CCD columns, and axis OX is perpendicular to the CCD[1]. Axis OZ might be inclined to the polar axis OZ' of the solar image by a small angle δP. Since the solar rotation axis is generally not in the plane of sky, there is an inclination of OZ' to Oz with an angle B_0, the maximum value of which is about 7°.25.

The spherical harmonics in the heliospheric coordinates can be expressed in terms of those in (r, Θ, Φ) coordinates:

$$Y_l^m(\theta, \phi) = \sum_{m'=-l}^{l} D^l_{m'm}(\alpha, \beta, \gamma) Y_l^{m'}(\Theta, \Phi), \tag{7}$$

where $D^l_{m'm}(\alpha, \beta, \gamma)$ is a rotation matrix (the Wigner D-function), and α, β and γ are Euler angles for a transformation from (r, θ, ϕ) to (r, Θ, Φ).

The line-of-sight velocity component is given by

$$v_{nlm;d} = \boldsymbol{v}_{nlm} \cdot \boldsymbol{e}_d, \tag{8}$$

where $\boldsymbol{e}_d = (\sin\Theta\cos\Phi)\boldsymbol{e}_r + (\cos\Theta\cos\Phi)\boldsymbol{e}_\Theta - (\sin\Phi)\boldsymbol{e}_\Phi$ is the unit vector along the line of sight. Then, from Eq. 5–8 we obtain the observed velocity in the coordinates associated with the CCD array:

$$\begin{aligned} v_{nlm;d} \;=\; & a_{nlm} e^{-i(\omega_{nlm}t + \epsilon_{nlm})} \sum_{m'=-l}^{l} D^l_{m'm} \left[Y_l^{m'}(\Theta, \Phi) \sin\Theta\cos\Phi + \right. \\ & \left. \frac{\alpha_{nlm'}}{\sqrt{l(l+1)}} \left(\frac{\partial}{\partial\Theta} Y_l^{m'}(\Theta, \Phi) \cos\Theta\cos\Phi - \frac{1}{\sin\Theta} \frac{\partial}{\partial\Phi} Y_l^{m'}(\Theta, \Phi) \sin\Phi \right) \right]. \end{aligned} \tag{9}$$

The binned data can be taken as averages of Doppler measurements from individual pixels. Then the oscillatory component in the data can be presented by

$$v_{\mathrm{osc};k} = \sum_{nlm} a_{nlm} e^{-i(\omega_{nlm}t + \epsilon_{nlm})} S_{lm;k}, \tag{10}$$

where $S_{lm;k}$ is a sensitivity function of a bin k to an eigenmode of degree l and order m. It is expressed in terms the sensitivity functions $S_{lm';k}$ computed in the coordinate system (Θ, Φ)

[1]In version 1.0 axis OY was chosen perpendicular to the CCD.

associated with the CCD array:

$$S_{lm;k} \equiv \sum_{m'=-l}^{l} D^l_{m'm} S_{lm';k}, \tag{11}$$

where

$$\begin{aligned} S_{lm';k} \;=\; & \int\int_k \Big[Y_l^{m'}(\Theta,\Phi)\sin\Theta\cos\Phi \;+ \\ & \frac{\alpha_{nlm'}}{\sqrt{l(l+1)}}\left(\frac{\partial}{\partial\Theta}Y_l^{m'}(\Theta,\Phi)\cos\Theta\cos\Phi \;- \right. \\ & \left.\left.\frac{1}{\sin\Theta}\frac{\partial}{\partial\Phi}Y_l^{m'}(\Theta,\Phi)\sin\Phi\right)\right]\sin^2\Theta\cos\Phi d\Theta d\Phi. \end{aligned} \tag{12}$$

For the data binning discussed in Section 2 the double integrals can be reduced to products of one-dimensional integrals:

$$\mathrm{Re}S_{lm';k} = \mathcal{T}^1_{lm'}\mathcal{F}^1_{m'} + \frac{\alpha_{nlm'}}{\sqrt{l(l+1)}}\left(\mathcal{T}^3_{lm'}\mathcal{F}^1_{m'} + m'\mathcal{T}^2_{lm'}\mathcal{G}^2_{m'}\right), \tag{13}$$

$$\mathrm{Im}S_{lm';k} = \mathcal{T}^1_{lm'}\mathcal{F}^2_{m'} + \frac{\alpha_{nlm'}}{\sqrt{l(l+1)}}\left(\mathcal{T}^3_{lm'}\mathcal{F}^2_{m'} - m'\mathcal{T}^2_{lm'}\mathcal{G}^1_{m'}\right), \tag{14}$$

where

$$\mathcal{T}^1_{lm} \equiv \int_{\Theta_k}^{\Theta_{k+1}} P_l^m(\cos\Theta)\sin^3\Theta d\Theta, \tag{15}$$

$$\mathcal{T}^2_{lm} \equiv \int_{\Theta_k}^{\Theta_{k+1}} P_l^m(\cos\Theta)\sin\Theta d\Theta, \tag{16}$$

$$\mathcal{T}^3_{lm} \equiv \int_{\Theta_k}^{\Theta_{k+1}} \frac{dP_l^m(\cos\Theta)}{d\Theta}\cos\Theta\sin^2\Theta d\Theta; \tag{17}$$

and

$$\mathcal{F}^1_m \equiv \frac{1}{\sqrt{2\pi}}\int_{\Phi_k}^{\Phi_{k+1}} \cos m\Phi\cos^2\Phi d\Phi, \tag{18}$$

$$\mathcal{F}^2_m \equiv \frac{1}{\sqrt{2\pi}}\int_{\Phi_k}^{\Phi_{k+1}} \sin m\Phi\cos^2\Phi d\Phi, \tag{19}$$

$$\mathcal{G}^1_m \equiv \frac{1}{\sqrt{2\pi}}\int_{\Phi_k}^{\Phi_{k+1}} \cos m\Phi\sin\Phi\cos\Phi d\Phi, \tag{20}$$

$$\mathcal{G}^2_m \equiv \frac{1}{\sqrt{2\pi}}\int_{\Phi_k}^{\Phi_{k+1}} \sin m\Phi\sin\Phi\cos\Phi d\Phi, \tag{21}$$

where Θ_k and Φ_k are coordinates of the bin boundaries. The integrals $\mathcal{T}^\lambda_{lm}$, $\mathcal{F}^\lambda_m$ and $\mathcal{G}^\lambda_m$ can be computed by using recurrence relations, derived in [14] (see Appendix).

3.2 Mode filtering

The next problem is to isolate signals

$$A_{lm} \equiv \sum_n a_{nlm} e^{-i(\omega_{nlm} t + \epsilon_{nlm})} \tag{22}$$

of oscillation modes of given l and m from the data. The amplitudes a_{nlm}, frequencies ω_{nlm} and phases ϵ_{nlm} of individual modes can be obtained from A_{lm} by a subsequent Fourier analysis. For A_{lm} we have a set of linear equations (cf. Eq. 10):

$$v_{d;k} = \sum_{lm} A_{lm} S_{lm;k} + v_{\mathrm{noise};k} \tag{23}$$

where $v_{d;k}$ is the Doppler velocity measured in the bin k: $k = 1, \ldots, K_{\mathrm{bin}}$, K_{bin} being the total number of bins. The measured velocities consist of the oscillatory signals $v_{\mathrm{osc};k}$ (Eq. 10) and $v_{\mathrm{noise};k}$, which include contributions from the other motions on the solar surface, like convection and rotation. We assume that the main part of the rotation signal has been taken out of the data[2].

It should be noted that an unique solution of the equations (23) is not possible, because the total number K_{bin} of the measurements $v_{d;k}$ is less than the total number of modes (with unknown amplitudes A_{lm}) contributing to $\sum_{lm} A_{lm} S_{lm;k}$. It is still impossible even with data of infinitesimal spatial resolution on the solar disk, because no more than even a hemisphere of the sun is observed.

Therefore, the linear system (23) is underdetermined, and a normal solution of it can be found under some additional constraints. The solution will satisfy Eq. (23) in a least-squares sense and will consist of a linear combination of A_{lm}. The task is of finding a solution that would allow us to isolate the signal $A_{l_0 m_0}$ for given l_0 and m_0 such that the amplitudes of most of the modes were significantly smaller than $A_{l_0 m_0}$ in the solution, and the frequencies of the remaining modes of similar amplitudes were different from the frequencies of the target modes, so the last could be easily identified in the power spectrum of $A_{l_0 m_0}$.

Several approaches to finding of $A_{l_0 m_0}$ from Eq. (23) have been considered. Gough and Latour [12], Christensen-Dalsgaard [13], and Appourchaux and Andersen [15] have discussed an optimally localized averaging technique, in which they put some explicit constraints

---

[2]One of the possibilities for removing rotation from the data (at least when angle δP is sufficiently small) is to take a symmetrical part (relative to the axis OZ') of the data as suggested in [12,14] by taking a sum of signals from symmetric pixels in the eastern and western parts of the solar image. In this case the modes with positive and negative values of m are not separated; that, however, can give an advantage for rotational frequency splitting measurements in power spectra of A_{lm}.

on harmonics that could interfere with the target modes. Kosovichev [14] has applied a regularized least-squares technique to find a pseudo-inverse matrix to $S_{lm;k}$. Libbrecht and Zirin [16] have employed an approximate orthogonality of the sensitivity functions $S_{lm;k}$, which results from the orthogonality of the spherical harmonics; they found that a simple projection technique was accurate enough for BBSO data analyses.

In this first version of the notes we consider some examples only for the projection technique applied to a non-uniform SOI mask. In the technique, an approximate solution of (23) is given by

$$\tilde{A}_{l_0m_0} = \frac{\sum_k S_{l_0m_0;k} v_{d;k}}{\sum_k |S_{l_0m_0;k}|^2}. \tag{24}$$

Unlike the two previous techniques, no attempt to reduce contamination of $A_{l_0m_0}$ by $v_{\rm noise}$ is made.

3.3 Results for the projection technique

Computations have been carried out for the mask shown in Figure 2. In the examples we assumed for simplicity that the angles B_0 and δP are both equal to zero, and that the horizontal component of the eigenfunctions is negligible ($\alpha_{nlm} = 0$). The purposes of the computations were to determine how well given modes could be isolated in the data, what value of $l_{\rm max}$ could be considered for the mask, and how serious the aliasing of target modes with higher-degree modes could be. Attention was paid mainly to the modes of intermediate azimuthal order $m \sim l/2$, for which the filtering was expected to be worse than for the modes of low ($m \sim 0$) and high ($m \sim l$) orders, as this particular mask was optimized for those modes.

The results are shown in Figures 3–10. In Figures $3a-c$ we illustrate the extraction of modes of $l_0 = 50$ and $m_0 = 0$ (Fig.3a), 20 (b) and 50 (c) from the data, assuming that all the harmonics are of equal amplitudes: $A_{lm} = 1$. In other words, we compute $\tilde{A}_{l_0m_0}$ by using (24) for $v_{d;k} = S_{lm;k}$, for different l and m, and plot the values of $\tilde{A}_{l_0m_0}$ in the $l-m$ plane. The positive values of $\tilde{A}_{l_0m_0}$ are shown by "pluses" and the negative ones, by "minuses", the sizes of the signs being proportional to the absolute values of $\tilde{A}_{l_0m_0}$.

For $l_0 = 100$ and $m_0 = 50$ we show only a part of the $l-m$ plane, in which $\tilde{A}_{l_0m_0}$ are of noticeable amplitudes. In this case there is a small-amplitude leakage into modes of smaller degree $l \simeq 80-90$.

For $l_0 = 200$ and $m_0 = 100$ (Figure 5) amplitudes of the leakage modes of $l \sim 170-180$ are comparable with the amplitudes of the target mode. However, the leakage modes can be separated from the target by Fourier analysis, because their frequencies are different, so

their peaks do not overlap in power spectra.

In Figures 6–9 we show values of $\sum_m \tilde{A}^2_{l_0 m_0}$, a measure of the spectral power of mode multiplets, as a function of l for $l_0 = 50$, $m_0 = 20$ (Fig.6); $l_0 = 100$, $m_0 = 50$ (Fig.7); $l_0 = 200$, $m_0 = 100$ (Fig.8) and $l_0 = 300$, $m_0 = 150$ (Fig.9). For large l_0 ($\gtrsim 200$) leakage modes might even have more power than a target mode. As we have mentioned, there is no problem in analysing modes up to $l_0 \simeq 200$, but for higher values of l_0 mode identification is not straightforward. However, since the mode structure of solar acoustic oscillations can be known, there is a possibility of studying the high-degree mode by analysing leakage peaks. For instance, the spectrum computed for $l_0 = 300$ can actually give us information about these modes despite of aliasing with higher l modes. Nevertheless, their analysis might be not standard, and we therefore set the maximum degree $l_{\max} = 200$ for modes that could be observed reliably with the mask. This limit can presumably be increased by using an optimal filtering technique instead of the projection technique.

Figure 10 shows leakage of power of a high-degree mode ($l = 300$) into the spectral power of lower-degree modes. As can be seen, the leakage does not produce any significant aliasing at $l \lesssim l_{\max}$.

The results shown in Figures 9 and 10 lead us to the suggestion that there is no necessity in smoothing the binned data (by applying a Gaussian filter, for instance), because aliasing with high-degree modes appears not to be significant, and, on the other hand, there is a possibility of observing oscillation modes beyond $l_{\max}$.

3.4 Corrections for angles B_0 and δP

In Sec. 3.1 it has been mentioned that (r, Θ, Φ) coordinates related to the solar image on the CCD do not necessarily coincide with the heliospheric coordinates (r, θ, ϕ), because the solar axis may be oriented not along the CCD columns, but with some small angle δP. Moreover, the solar axis is tilted from the plane of the detector with angle B_0, because the solar axis is not exactly perpendicular to the ecliptic. Both δP and B_0 are changed with time. Thus some correction of the procedure for the angles is needed.

One of the solutions is in remapping the CCD pixels onto the heliospheric coordinates [18] in order to keep the bin configuration approximately the same in the coordinates. Another possibility is in using the bins fixed in time, and in correcting the numerical filters $S_{l_0,m_0;k}$ (24), which are applied to the bin signals to extract the eigenfunctions of given l_0 and m_0. The numerical corrections can be included in a data processing pipeline on the ground. It is important that in this case knowledge of the precise values of B_0 and δP is not required: they can be adjusted iteratively.

As shown in Sec. 3.1 the sensitivity functions $S_{l,m;k}$ for non-zero δP and B_0 are transformed according to (11). In the equation the Wigner D-functions are defined by the Euler angles α, β and γ [see Appendix A.3]. In our case $\alpha = \gamma = 0$ and $\cos\beta = \cos B_0 \cos \delta P$. Since δP is expected to be less than $0°.5$, it is less significant than B_0, which may be as large as $7°$. The procedure for the corrections by means of the D-functions is precise only in the case of exact orthogonality of the eigenfunctions, which cannot be achieved in practice, because only a hemisphere of the sun is observed. However, one can expect the procedure to provide approximate corrections, which can be tested numerically.

In Figure 11 we show the results of extraction of the modes of $l_0 = 100$ and $m_0 = 50$ when $B_0 = 7°$. Comparing with the results for $B_0 = 0$ (Figure 4) one can see small additional aliasing with modes of $l \simeq 55$ and $m \simeq 50$. The corresponding "power" spectra $\sum_m \tilde{A}^2_{lm}$ are shown in Figure 12.

Figures $13a - c$ demonstrate the extraction of the zonal harmonics ($l_0 = 200, m_0 = 0$) at $B_0 = 0$ (a) and $7°$ (b). Similar results for the sectoral modes ($l_0 = 200, m_0 = 200$) are shown in Figures $15a - c$. In both cases the procedure for the numerical corrections works well. However, extracting intermediate-order modes of $l_0 = 200$ and $m_0 = 100$, we found a noticeable aliasing with modes of $l \simeq 100$ when $B_0 \neq 0$ (Figures $14a - c$). Significance of the aliasing for mode frequency measurement can be assessed only by full-scale simulations including Fourier analysis of time series. However, the amplitudes of the aliasing modes can be reduced by optimizing the bin structure of the masks.

4 Conclusion

Spatially non-uniform data binning can be used as an effective technique for the SOI Structure Program to observe all p modes of degree l up to $l_{\max} \sim 2\sqrt{K_{\rm bin}}$ with minimal data processing on board. Most of the data processing of the binned data can be accomplished on the ground by an optimal filtering technique, taking into account corrections for the inclination of the solar axis, for eigenfunction distortions, and for systematic and random sources of noise. The corrections for the inclination of the solar axis have been considered in the present version of the notes. We plan to study the other effects in future versions.

Acknowledgements

I am very grateful to Thierry Appourchaux, Lyle Bacon, Douglas Gough, Peter Milford, Eva Novotny, Takashi Sekii and Phil Scherrer for useful discussions and suggestions.

Appendix

A.1. Associated Legendre functions The normalized associated Legendre functions $P_l^m(\mu)$, where $\mu = \cos\theta$, are computed by the following recurrence relations. First, for sectoral harmonics with $m = l$, we have

$$P_0^0(\mu) = \frac{1}{\sqrt{2}}; \tag{25}$$

$$P_m^m(\mu) = \left(1 + \frac{1}{2m}\right)^{\frac{1}{2}} \left(1 - \mu^2\right)^{\frac{1}{2}} P_{m-1}^{m-1}(\mu), \quad m = 1, 2, \ldots . \tag{26}$$

Then for $l > m$ we use

$$P_l^m(\mu) = a_{lm}\mu P_{l-1}^m(\mu) - b_{lm}P_{l-2}^m(\mu), \quad l = m+1, m+2, \ldots , \tag{27}$$

where

$$a_{lm} = \left(\frac{4l^2 - 1}{l^2 - m^2}\right)^{\frac{1}{2}}, \tag{28}$$

$$b_{lm} = \left[\frac{2l+1}{2l-3}\,\frac{(l-m-1)(l+m-1)}{(l+m)(l-m)}\right]^{\frac{1}{2}}. \tag{29}$$

For $l < m$ we set $P_l^m(\mu) = 0$.

A.2. Integrals of Associated Legendre Functions The integrals (15)-(17) can be expressed in terms of indefinite integrals

$$\mathcal{Q}_{lm}^{\lambda}(\mu) = \int P_l^m(\mu)\mu^{\lambda}d\mu \tag{30}$$

and

$$\mathcal{P}_{lm}^{\lambda}(\mu) = \int \frac{dP_l^m(\mu)}{d\mu}\mu^{\lambda}d\mu, \tag{31}$$

where $\mu = \cos\Theta$. The integrals can be effectively computed by using the following recurrence relations, derived in [14]:

$$\mathcal{Q}_{m,m}^0 = \alpha_m I_m, \tag{32}$$

where

$$I_0 = \mu, \quad I_1 = \frac{1}{2}\left[\mu\sqrt{1-\mu^2} + \arcsin\mu\right],$$

$$I_m = \frac{1}{m+1}\left[\mu(1-\mu^2)^{\frac{m}{2}} + mI_{m-2}\right], \quad m = 2, 3, \ldots ;$$

$$\alpha_0 = \sqrt{2}, \quad \alpha_m = \alpha_{m-1}\sqrt{1 + \frac{1}{2m}}, \quad m = 1, 2, \ldots .$$

$$\mathcal{Q}^0_{1,0} = \frac{1}{\sqrt{2}}\sqrt{1-\mu^2}P^1_1, \tag{33}$$

$$\mathcal{Q}^0_{m+1,m} = \frac{1}{m+2}\sqrt{\frac{2}{2m+1}}\sqrt{1-\mu^2}\left(P^{m-1}_{m+1} - \sqrt{m(2m+3)}P^{m-1}_{m-1}\right), \quad m = 1,2,\ldots; \tag{34}$$

$$\mathcal{Q}^0_{lm} = \frac{1}{l+1}\left[(l-2)b_{lm}\mathcal{Q}^0_{l-2,m} + \sqrt{1-\mu^2}\left(c_{lm}P^{m-1}_l + d_{lm}P^{m-1}_{l-2}\right)\right], \quad l = m+2, m+3, \ldots; \tag{35}$$

$$\mathcal{Q}^{\lambda+1}_{l-1,m} = \frac{1}{2a_{lm}}\left(\mathcal{Q}^{\lambda}_{lm} + \mathcal{Q}^{\lambda}_{l-2,m}\right), \quad m = 0,1,\ldots; \quad l = m+2, m+3, \ldots; \quad \lambda = 0,1,\ldots; \tag{36}$$

$$\mathcal{P}^{\lambda+1}_{l,m} = \mu^{\lambda+1}P^m_l - (\lambda+1)\mathcal{Q}^{\lambda}_{lm}, \quad m = 0,1,\ldots; \quad l = m, m+1, \ldots; \quad \lambda = 0,1,\ldots. \tag{37}$$

Here, the coefficients a_{lm} and b_{lm} are given by Eqs (28) and (29), and c_{lm} and d_{lm}, by

$$c_{lm} = \sqrt{\frac{l-m+1}{l+m}}, \tag{38}$$

$$d_{lm} = \left[\frac{2l+1}{2l-3}\,\frac{(l+m-1)(l+m-2)}{(l+m)(l-m)}\right]^{\frac{1}{2}}. \tag{39}$$

A.3. Wigner D-functions The Wigner D-functions $D^l_{m'm}(\alpha,\beta,\gamma)$ are represented by a product of three functions, each of them being a function of one argument α, β or γ:

$$D^l_{m'm}(\alpha,\beta,\gamma) \equiv e^{-im'\alpha}d^l_{m'm}(\beta)e^{-im\gamma}, \tag{40}$$

where $d^l_{m'm}(\beta)$ is a generalized spherical function. It can be computed by the following recurrence relations:

$$d^0_{0,0}(\mu) = 1; \quad d^m_{m,m}(\mu) = 0.5(1+\mu)d^m_{m-1,m-1}(\mu), \quad m = 1,2,\ldots,l_0; \tag{41}$$

$$d^m_{m,m'}(\mu) = \sqrt{\frac{m+m'+1}{m-m'}}\sqrt{\frac{1-\mu}{1+\mu}}d^m_{m,m'+1}(\mu), \quad m' = m, m-1, \ldots, -m, \quad m = 1,2,\ldots,l_0; \tag{42}$$

$$a_l d^{l+1}_{m,m'}(\mu) + b_l d^l_{m,m'}(\mu) + c_l d^{l-1}_{m,m'}(\mu) = \mu d^l_{m,m'}(\mu), \tag{43}$$

where

$$a_l = \frac{\sqrt{(l+m'+1)(l-m'+1)(l+m+1)(l-m+1)}}{(2l+1)(l+1)},$$

$$b_l = \frac{mm'}{l(l+1)},$$

$$c_l = \frac{\sqrt{(l+m')(l-m')(l+m)(l-m)}}{(2l+1)l},$$

and

$$l = m, m+1, \ldots, l_0, \qquad m' = m, m-1, \ldots, -m, \qquad m = 1,2,\ldots,l_0.$$

REFERENCES

1. Instrument Performance Specification for the SOI-MDI (eds. T.Hoeksema, I.Zayer), 1991, Revision 2, LARP: MDI 330016.

2. Gough, D.O. 1990, Comments on helioseismic inference, in: *Progress in Seismology of the Sun and Stars*, eds. Y.Osaki and H.Shibahashi, Springer, Berlin, p.283-318.

3. Libbrecht, K.G. and Kaufman J.M. 1988, Frequencies of high-degree solar oscillations, *apj*, **324**, 1172-83.

4. Kosovichev, A.G., Christensen-Dalsgaard, J., Däppen, W., Dziembowski, W., Gough, D.O, and Thompson, M.J. 1992, Sources of uncertainty in direct seismological measurements of the solar helium abundance, *M.N.R.A.S.*, in press

5. Däppen, W., Gough, D.O, Kosovichev, A.G. and Thompson, M.J., 1991, A new inversion for the hydrostatic stratification of the sun, in *Challenges to Theories of the Structure of Moderate-Mass Stars*, ed. D.O.Gough & J.Toomre, *Lect. Not. Phys.*. Heidelberg: Springer, p.111.

6. Kosovichev, A.G. 1992, Solar structure inversion package, SOI-MDI Technical Notes, SOI-TN-084.

7. Korzennik, S. 1990, Seismic analysis of the sun from intermediate and high degree p-modes. UCLA. Thesis.

8. Libbrecht, K.G., Woodard M.F. and Kaufman J.M. 1990, Frequencies of solar oscillations, *Ap.J.Suppl.*, **74**, 1129-49.

9. Duvall, T. 1992. Remark at SOI meeting. Boulder (August 1992).

10. Harvey, J. and the GONG Instrument Development Team, 1988, The GONG instrument, in: *Seismology of the sun & sun-like stars*, (ed. E.J.Rolfe). ESA Publ. SP-286, p.203-208.

11. Gough, D.O., Kosovichev, A.G., Sekii, T., Libbrecht, K.G., and Woodard, M.F. 1992, The form of the angular velocity in the solar convection zone, in Proc. GONG-92 conf. *Seismic investigation of the sun and stars*, (ed. T.Brown), in press.

12. Gough, D.O. and Latour, J., 1984, On the identification of normal modes of oscillation from observations of the solar periphery, *Astron. Expr.*, **1**, 9-25.

13. Christensen-Dalsgaard, J. 1984, Optimized response function for two-dimensional observations of solar oscillations, in: *Solar Seismology from Space*. (eds. R.K.Ulrich, J.Harvey, E.J.Rhodes,Jr and J.Toomre). JPL Publ. 84-84, p.219-54.

14. Kosovichev, A.G. 1987, Processing photo-diode array solar-oscillation observations, *Bull. Crimean Astr. Obs.*, **75**, 19-29.

15. Appourchaux, T. and Andersen, B.N., 1990, Observations of low-degree solar oscillations with few detector elements, *Solar Physics*, **128**, 91-110.

16. Libbrecht, K.G. and Zirin, H. 1986, Properties of intermediate-degree solar oscillation modes *Astrophys.J.* **308**, 413-423.

17. Christensen-Dalsgaard, J. and Gough, D.O., 1982, On interpretation of five-minute oscillations in solar spectrum line shifts, *Mon. Not. R. astr. Soc.*, **198**, 141-171.

18. Bacon, L., 1991, Remapping Equations, SOI-MDI Technical Notes, SOI-TN-027.

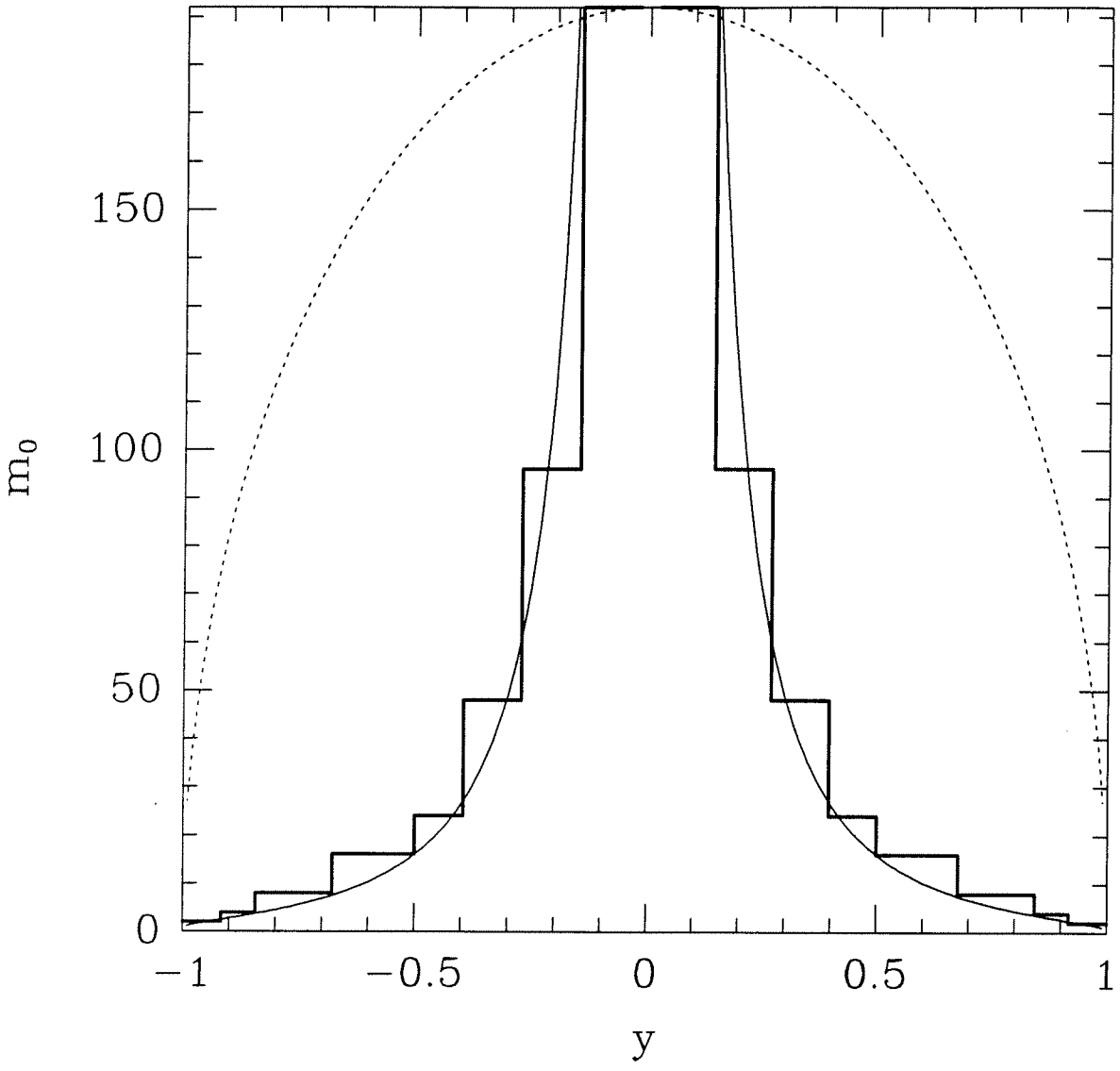

Figure 1

Oct 27 15:38:08 1992

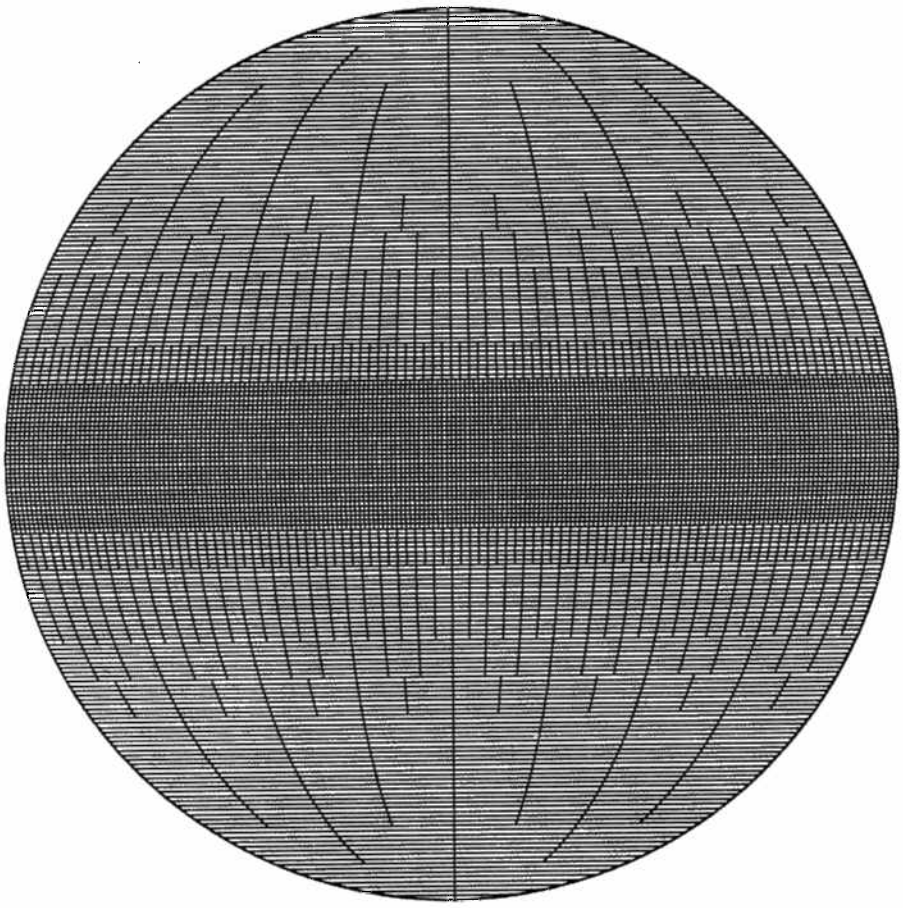

Figure 2

Oct 7 21:49:57 1992

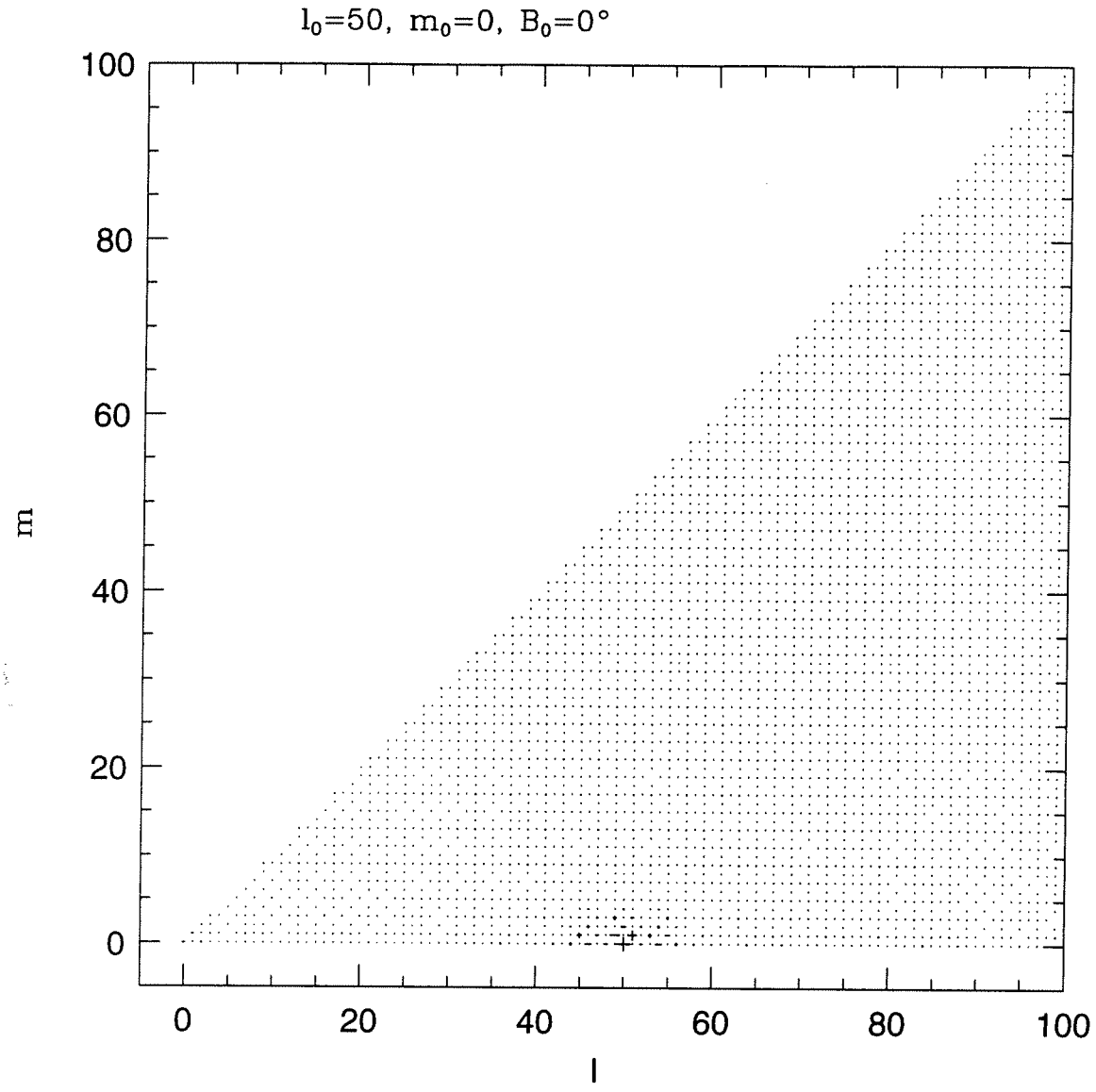

Figure 3a

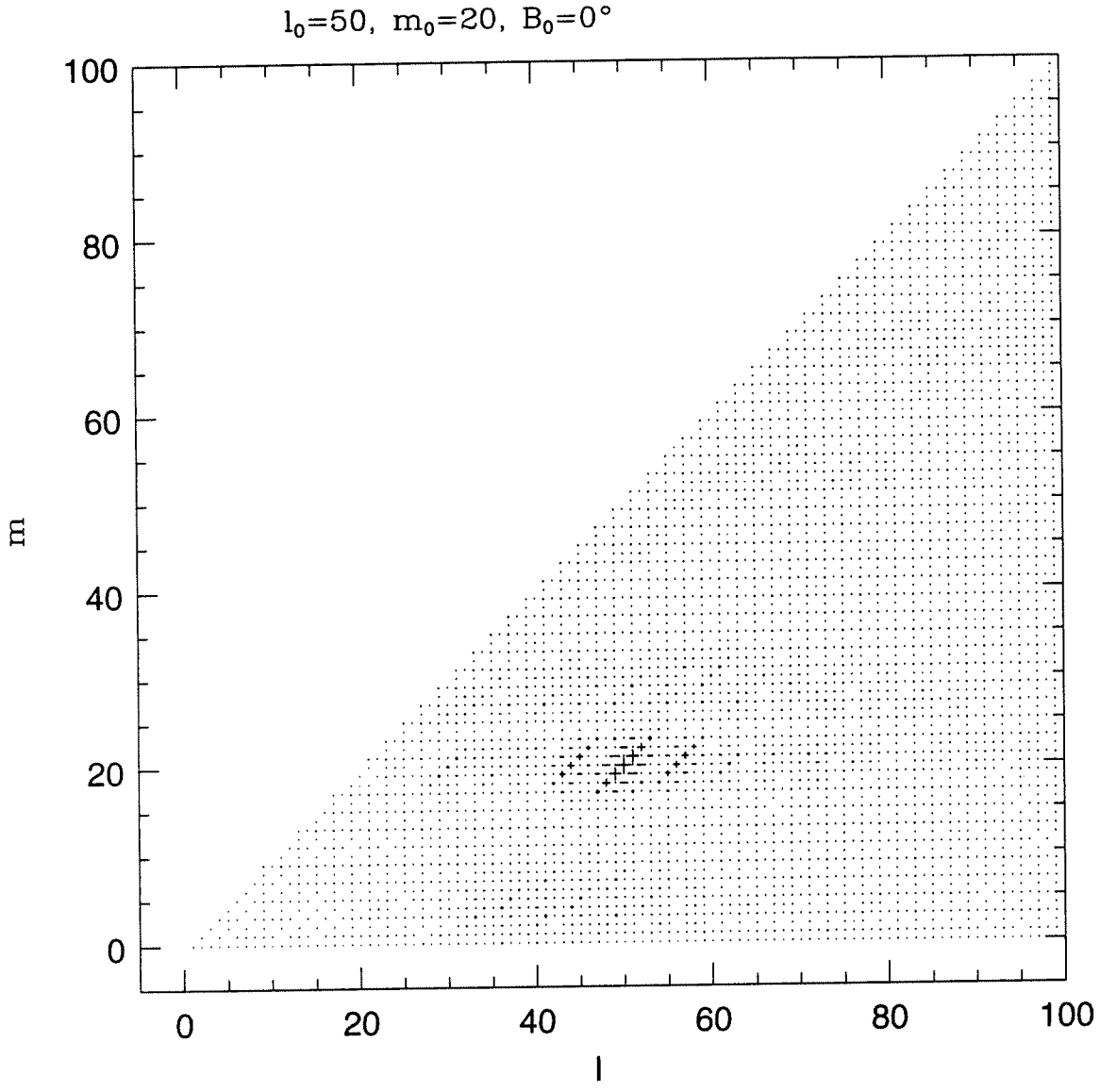

Figure 3b

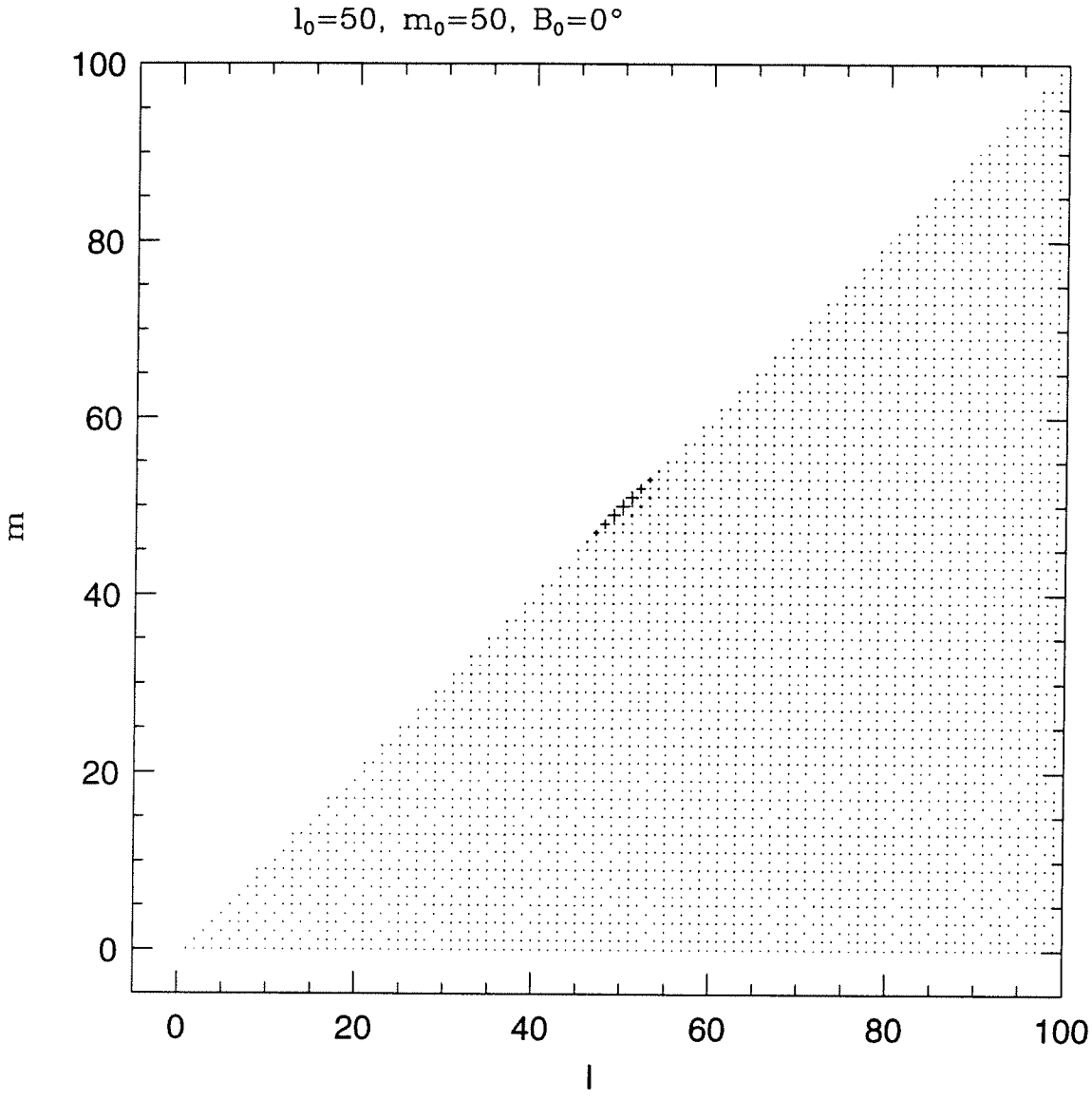

Figure 3c

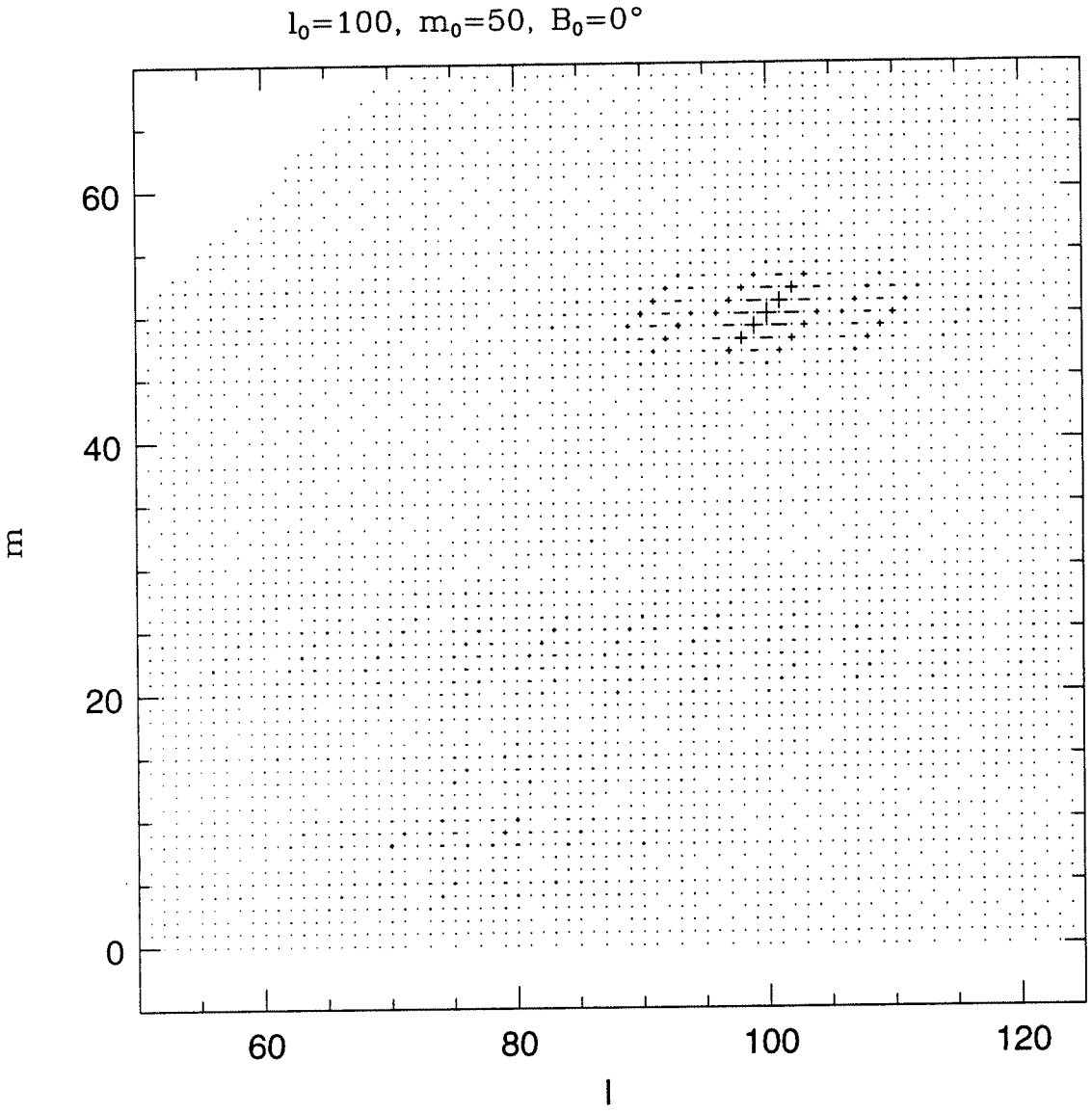

Figure 4

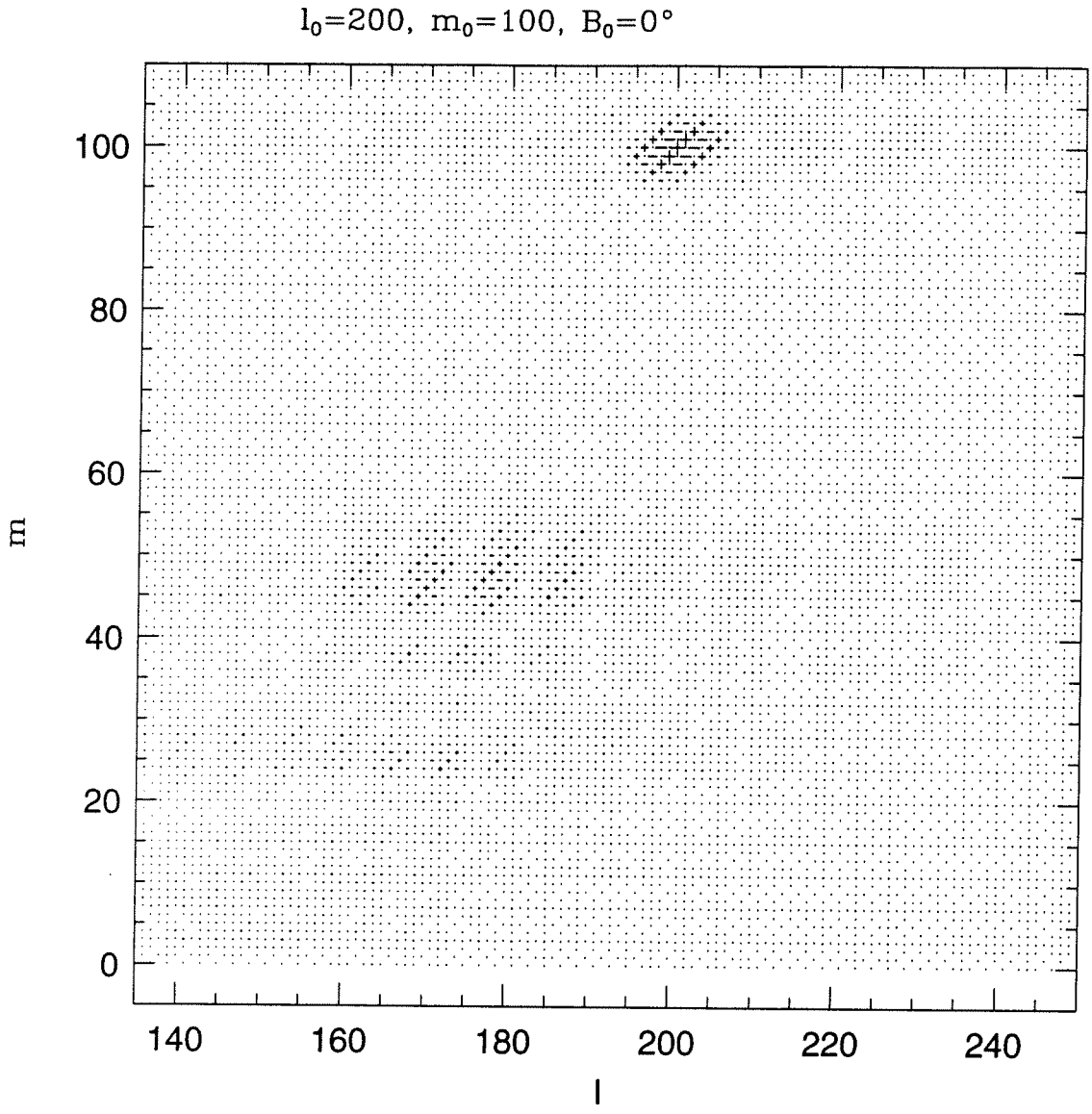

Figure 5

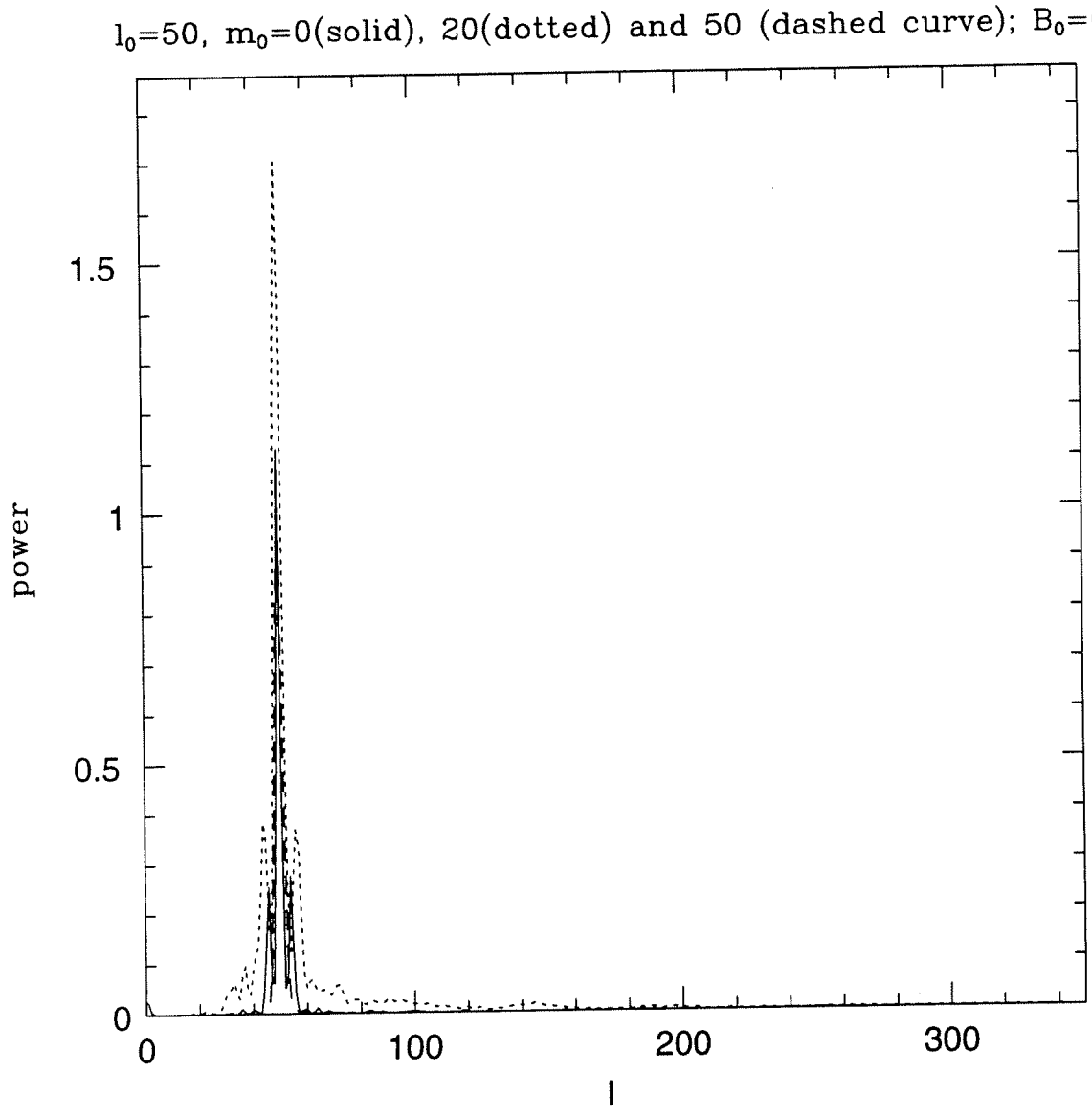
l_0=50, m_0=0(solid), 20(dotted) and 50 (dashed curve); B_0=0°
power
1.5
1
0.5
0
0
100
200
300
l

Figure 6

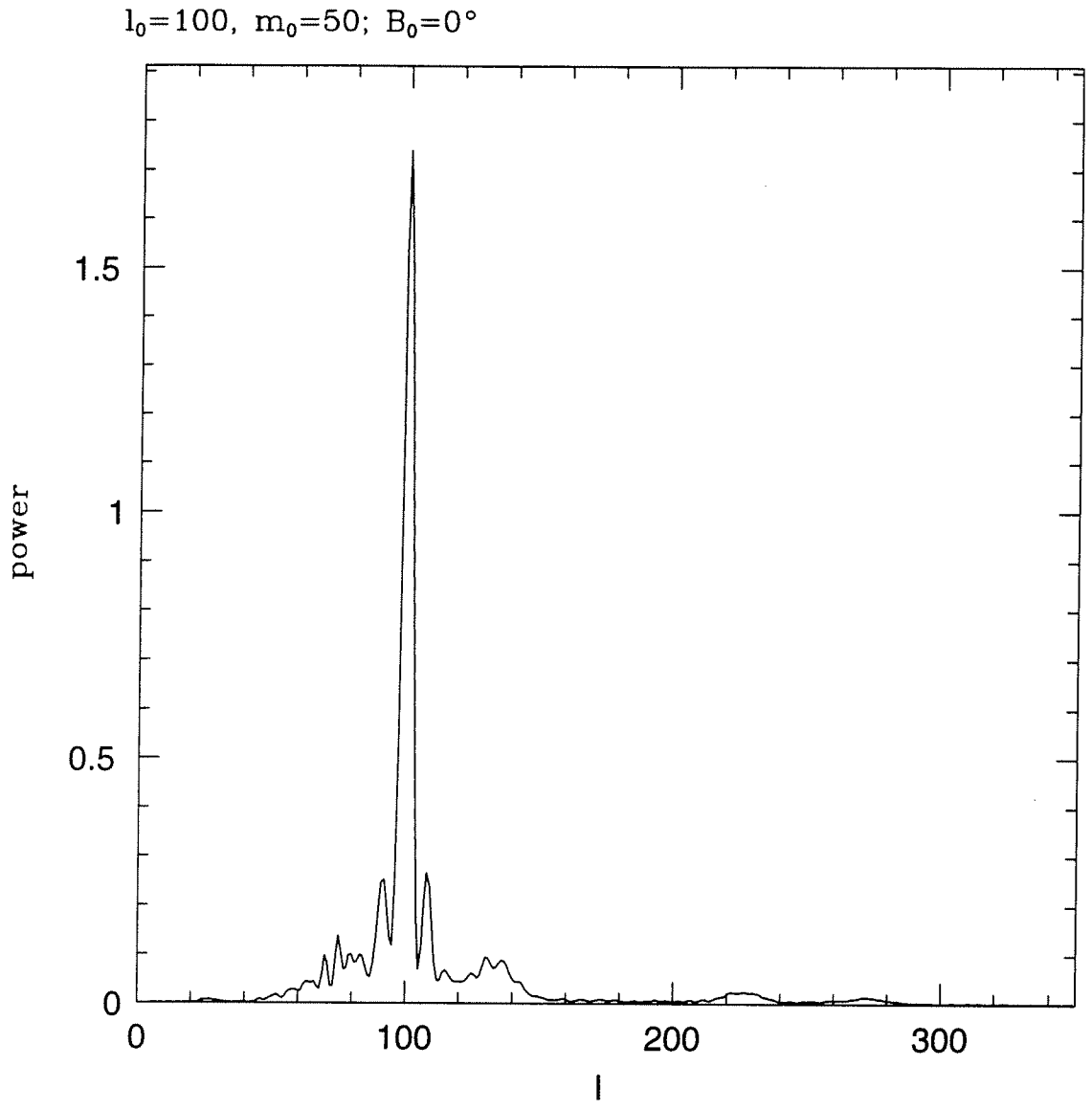

Figure 7

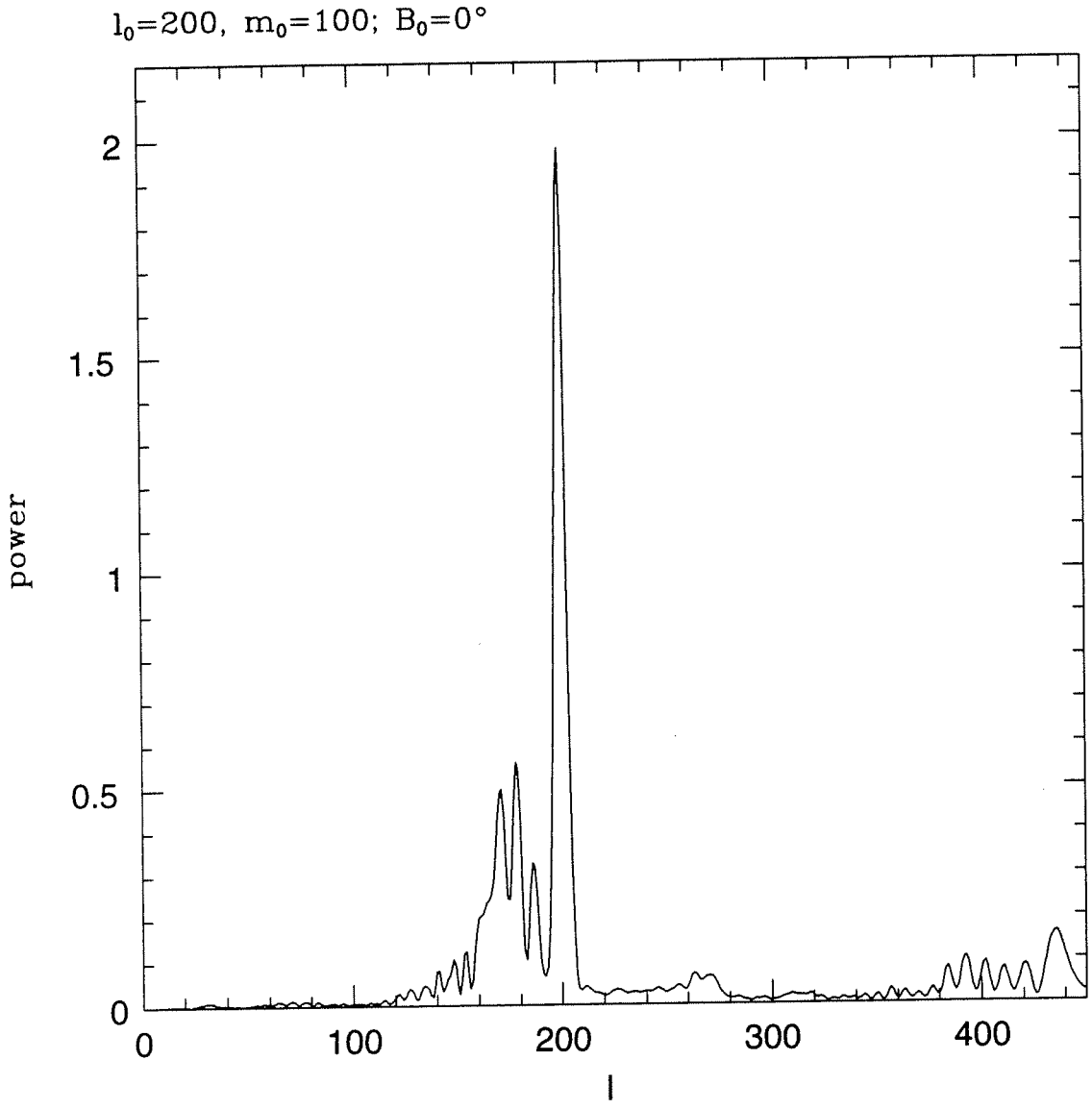

Figure 8

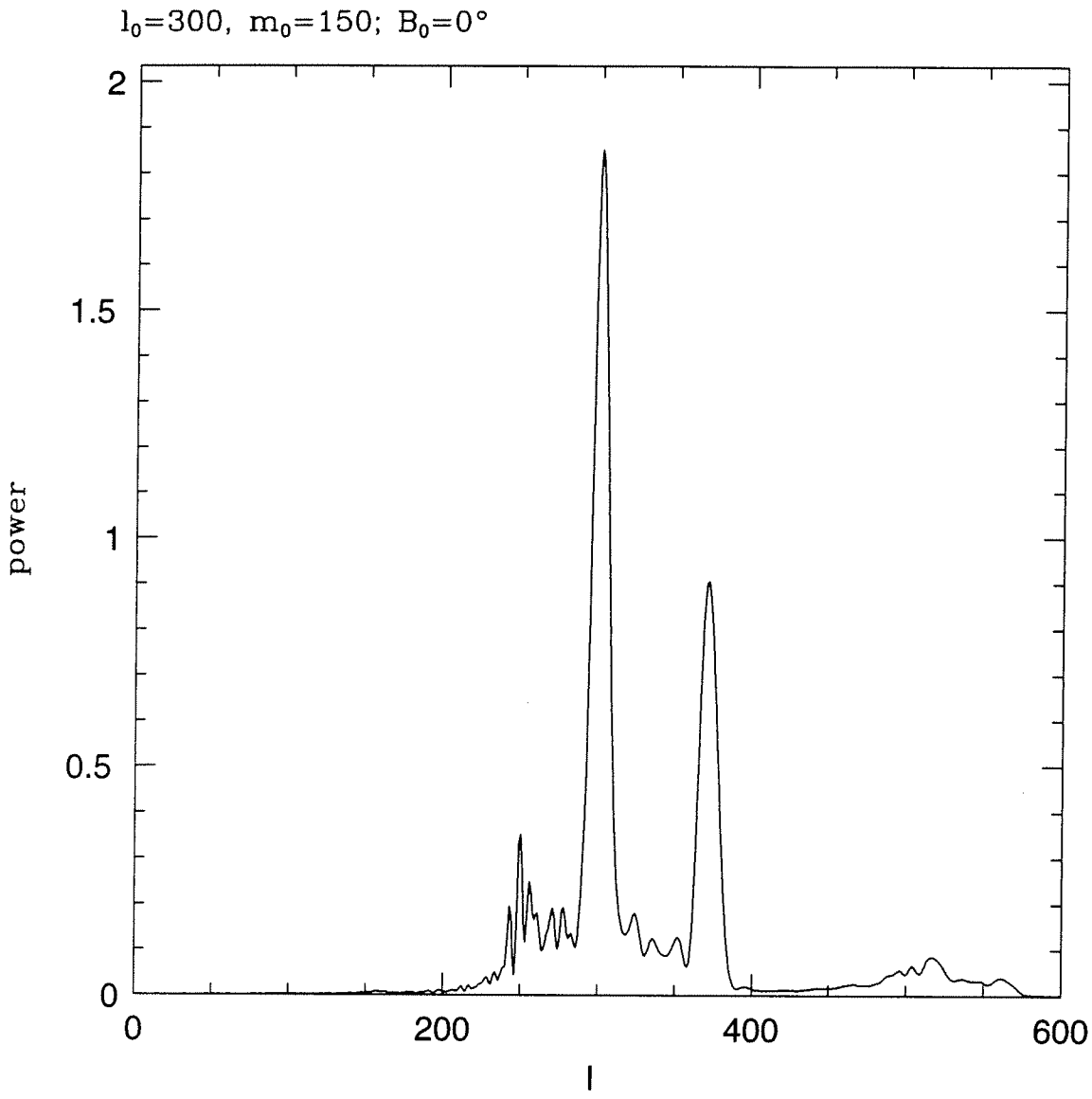

Figure 9

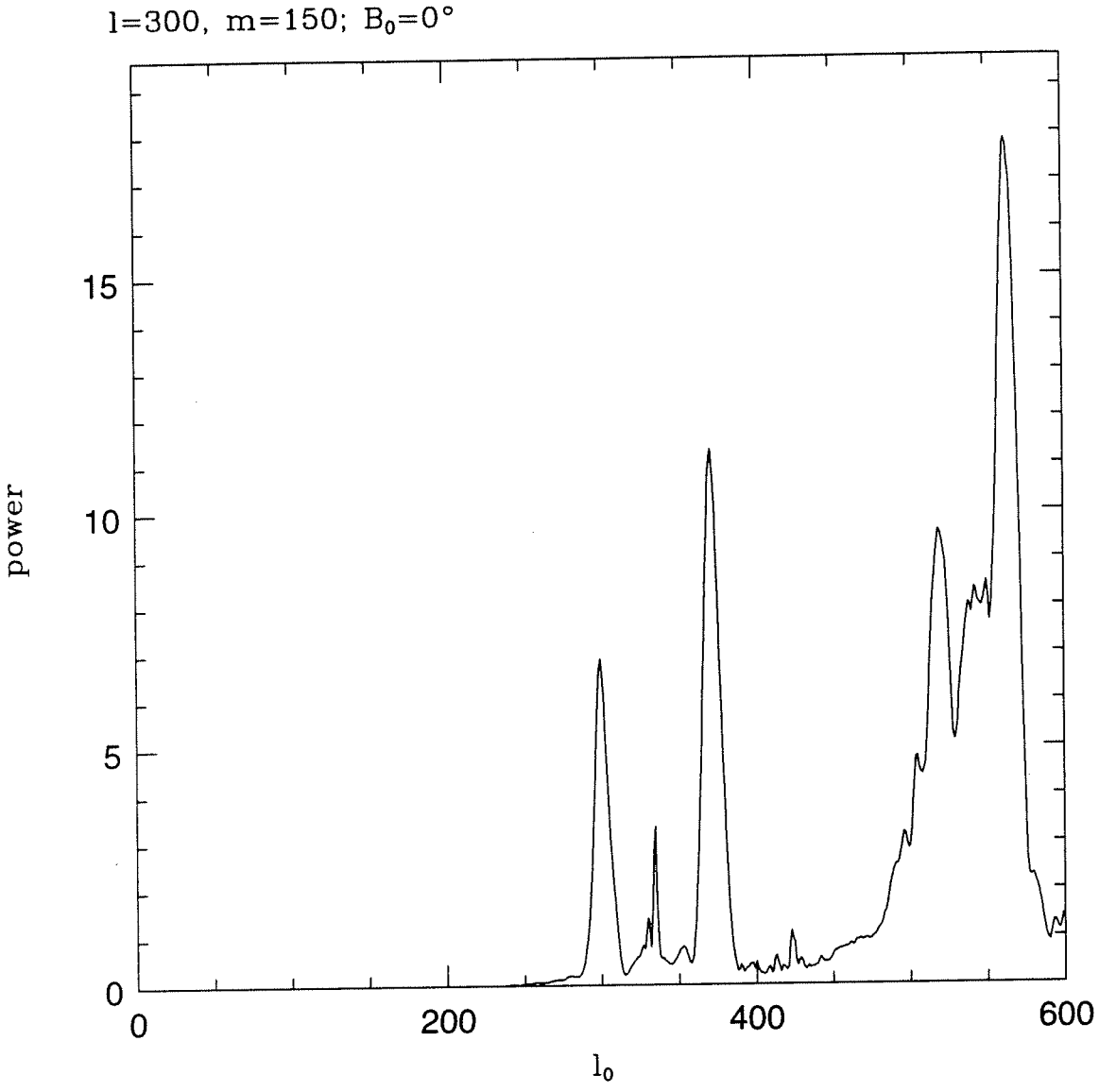

Figure 10

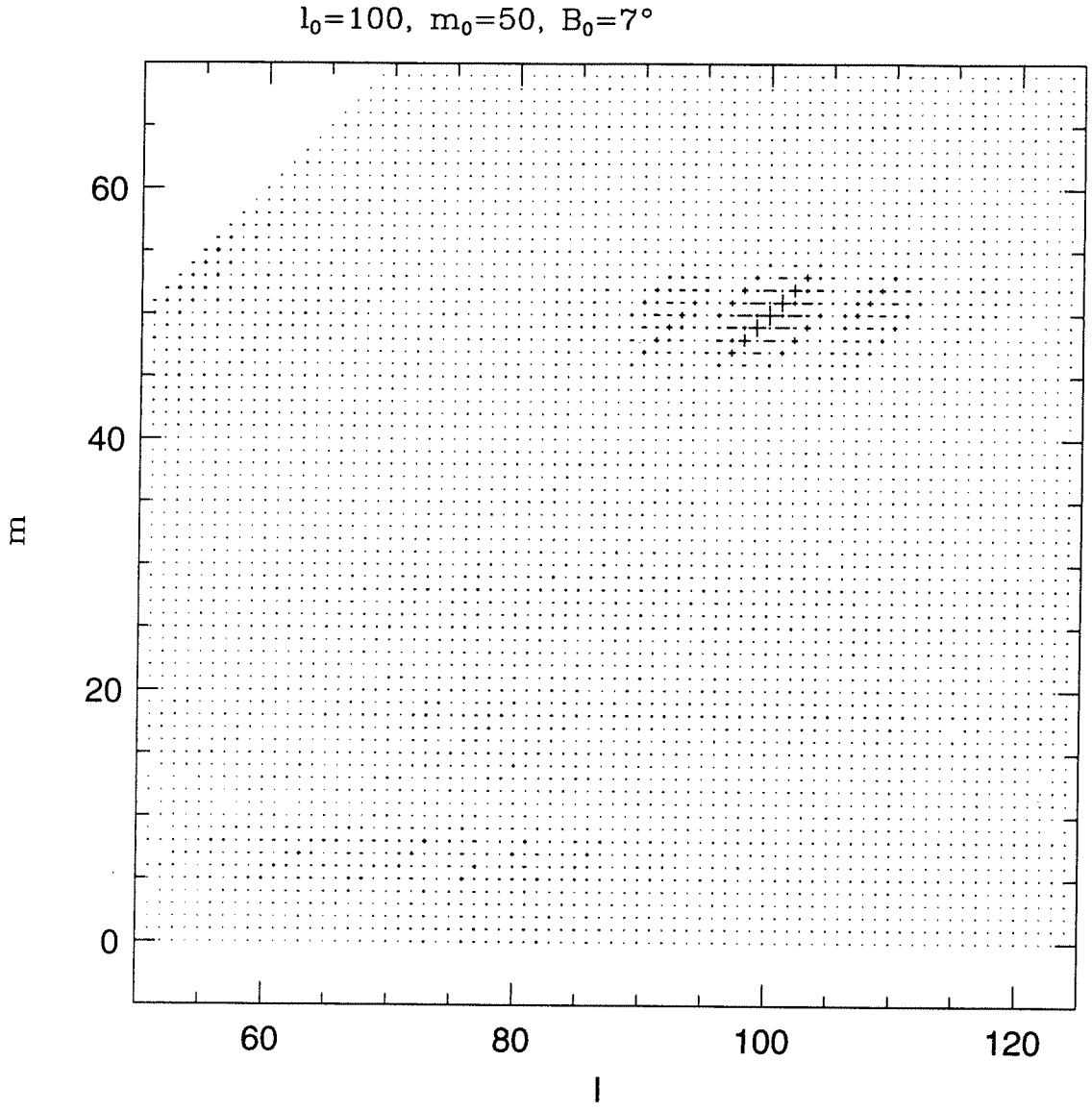

Figure 11

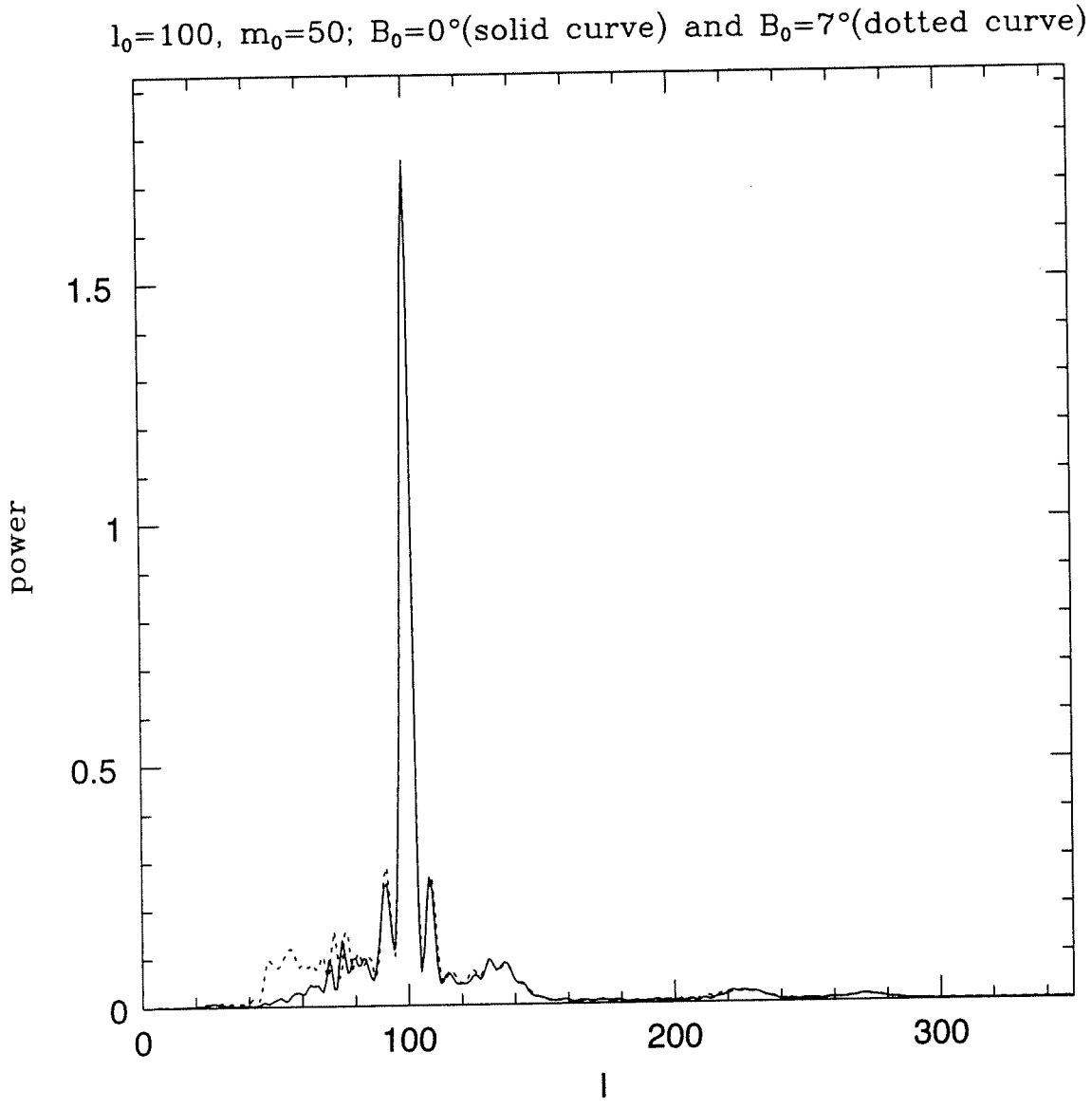
l_0=100, m_0=50; B_0=0°(solid curve) and B_0=7°(dotted curve)
power
1.5
1
0.5
0
0
100
200
300
l

Figure 12

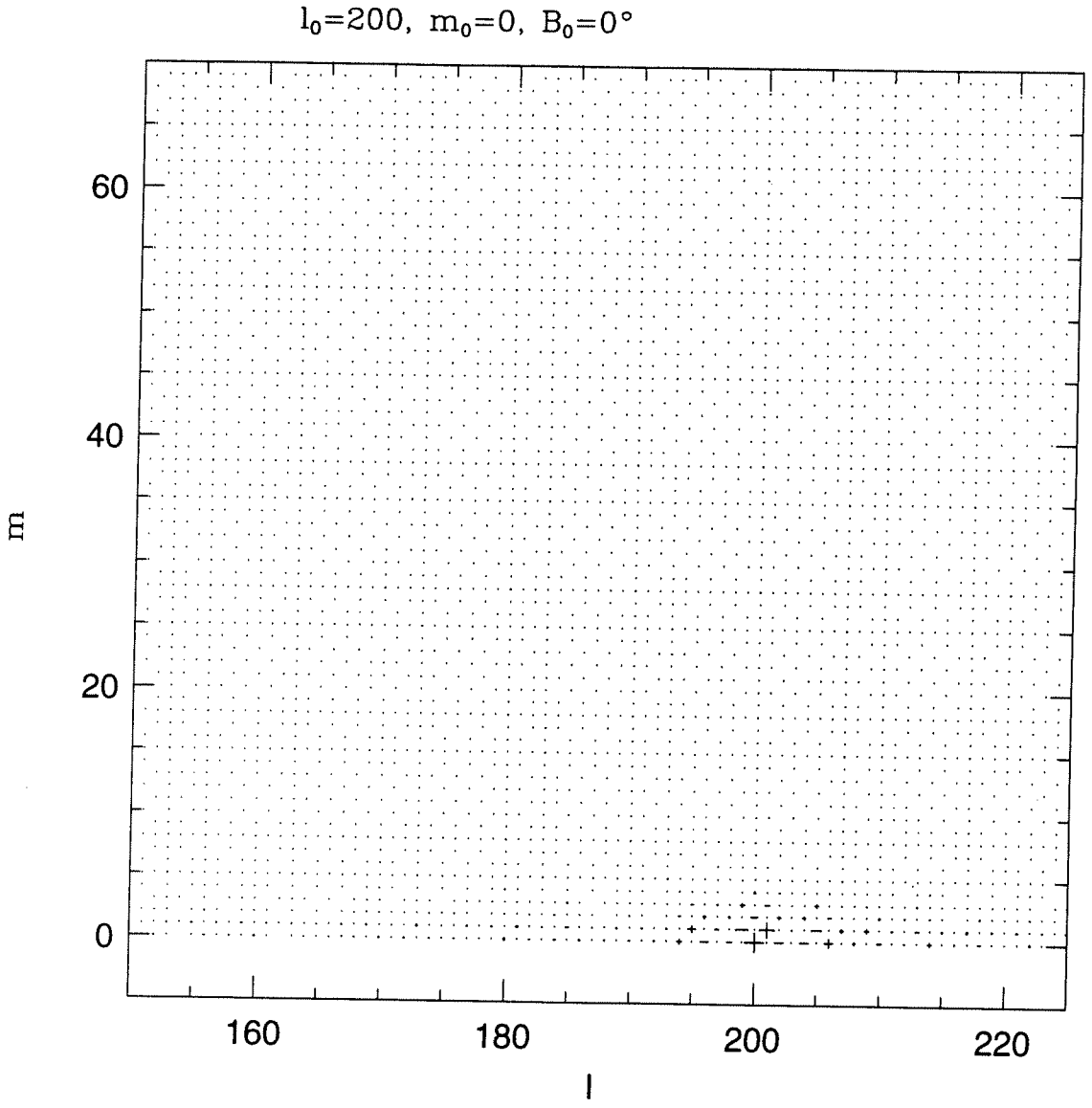

Figure 13a

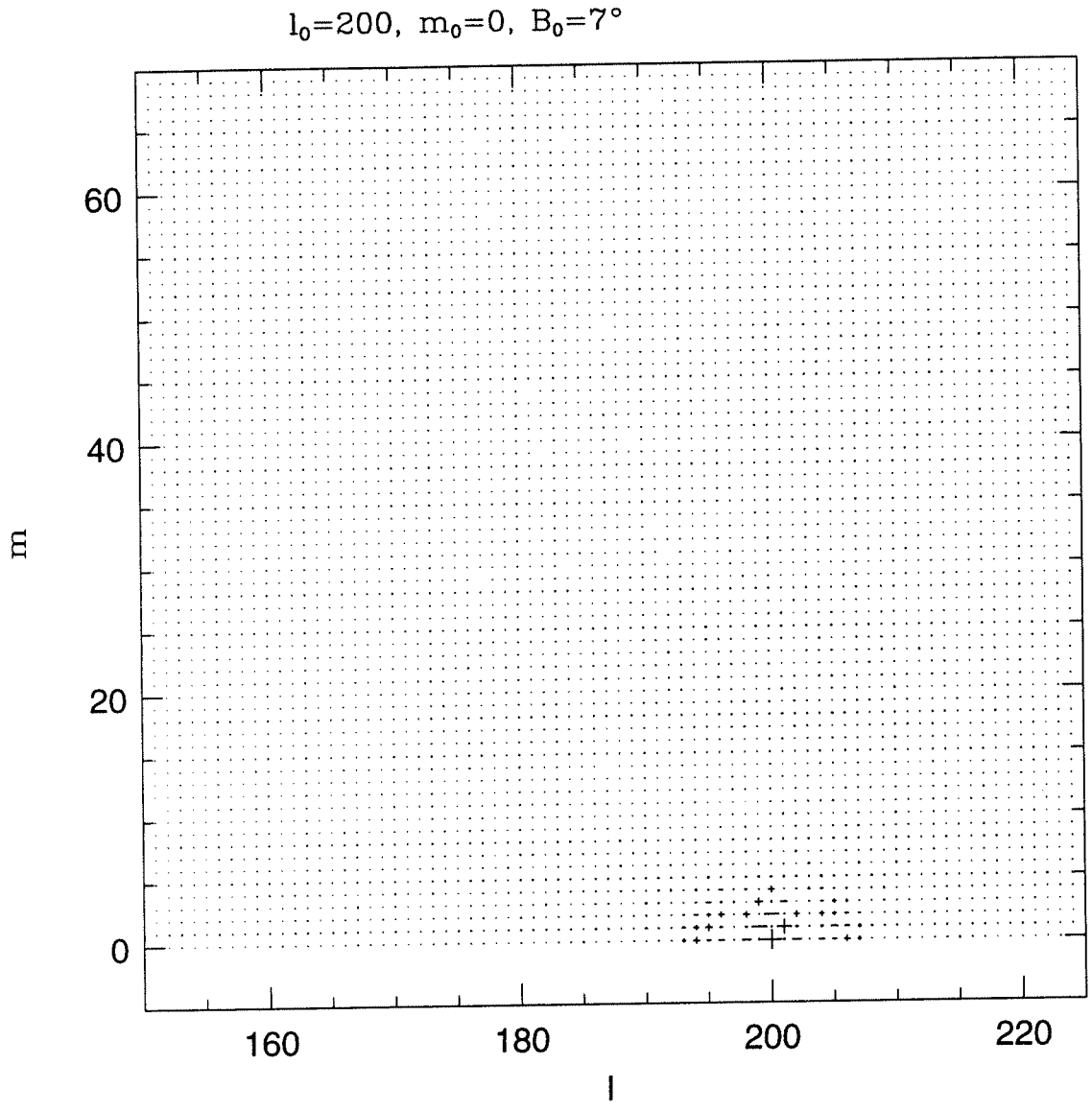

Figure 13b

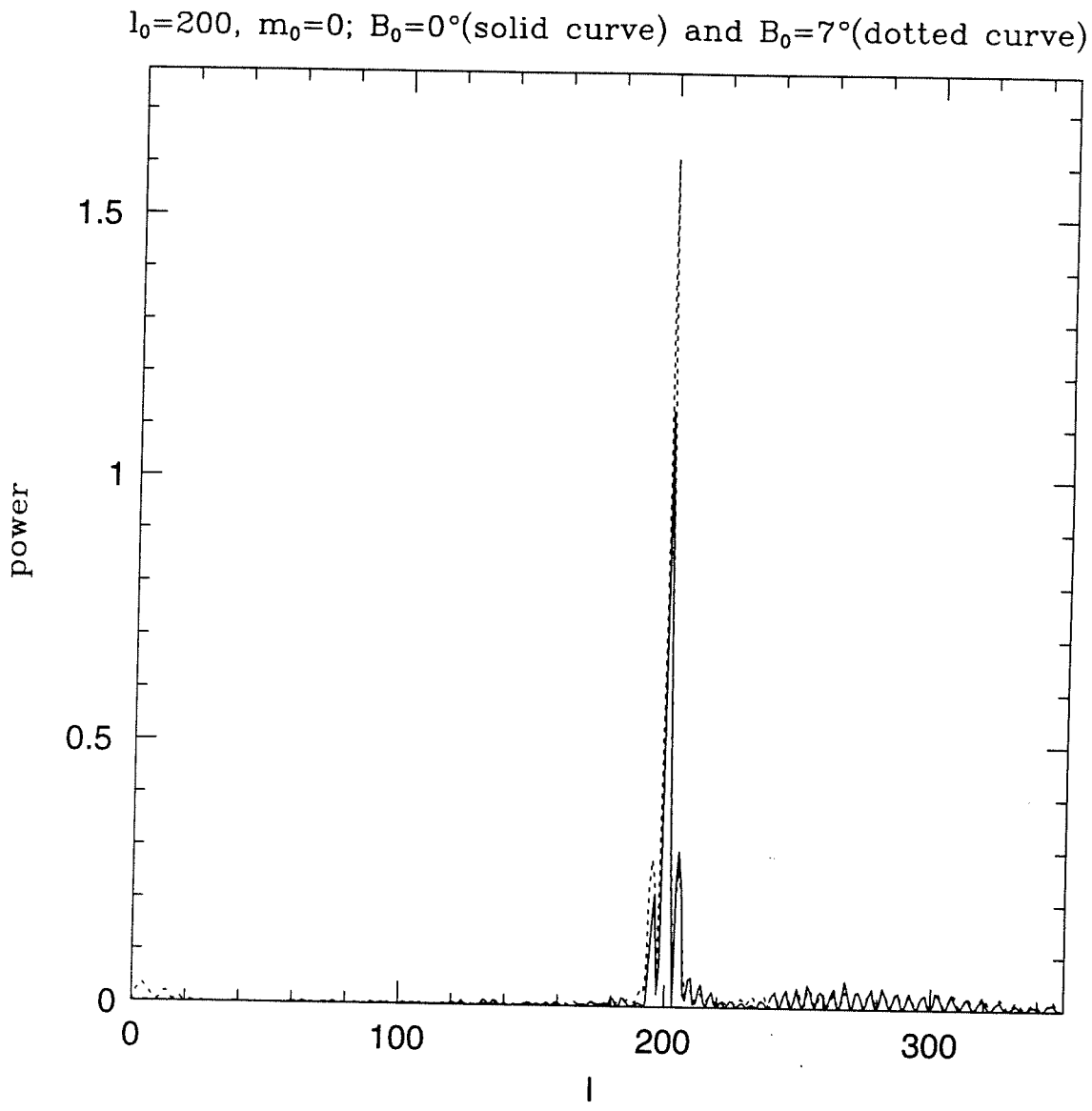
l_0=200, m_0=0; B_0=0°(solid curve) and B_0=7°(dotted curve)
power
1.5
1
0.5
0
0
100
200
300
l

Figure 13c